A Long-Term Shift in Flow Regimes over the Antarctic Peninsula

MARIA-VITTORIA GUARINO,[a,b,c] JEFF K. RIDLEY,[d] STEVE COLWELL,[b] RICCARDO FARNETI,[c] GRAZIANO GIULIANI,[c] NEIL HINDLEY,[e] JOHN KING,[b] FRED KUCHARSKI,[c] INNA POLICHTCHOUK,[f] ADRIAN MARK TOMPKINS,[c] ÉTIENNE VIGNON,[g] AND CORWIN WRIGHT[e]

[a] *Climate Modelling Division (SSPT-CLIMAR), ENEA, Rome, Italy*
[b] *British Antarctic Survey, Cambridge, United Kingdom*
[c] *Earth System Physics, International Centre for Theoretical Physics, Trieste, Italy*
[d] *Met Office, Exeter, United Kingdom*
[e] *Centre for Climate Adaptation and Environmental Research, University of Bath, Bath, United Kingdom*
[f] *ECMWF, Reading, United Kingdom*
[g] *Laboratoire de Météorologie Dynamique, IPSL, Sorbonne Université/CNRS/Ecole Normale Supérieure-PSL Université/Ecole Polytechnique-Institut Polytechnique de Paris, Paris, France*

(Manuscript received 12 June 2025, in final form 23 October 2025, accepted 24 November 2025)

ABSTRACT: Surface warming in the polar regions has important consequences for the stability of the lowest layers of the atmosphere and for atmospheric vertical movement. Here, using ERA5 reanalysis data and in situ measurements, we quantify the evolving static stability of the lowest 1 km of the Antarctic atmosphere and show that the Brunt–Väisälä frequency, a measure of atmospheric stability, has been steadily decreasing since the 1950s. Using satellite observations, reanalysis, and targeted climate simulations, we find that this reduced stability has prompted a shift in prevailing flow regimes over the Antarctic Peninsula by altering regional wind flow and enhancing the generation of orographic gravity waves. Increased gravity wave forcing from the Antarctic Peninsula can have important implications for global-scale circulation, polar vortex strength, ozone depletion, and midlatitude weather.

SIGNIFICANCE STATEMENT: We present consequences of Antarctic surface warming for the stability of the lower atmosphere since the 1950s. We show that the surface atmosphere over the Antarctic Peninsula has become less stable, and that this reduced stability favors the generation of atmospheric gravity waves from the Peninsula, one of the major sources of atmospheric waves on the planet. We provide a physically based explanation (i.e., a shift in flow regimes) for the increased gravity wave forcing that we find in an unprecedented set of reanalysis products, satellite observations, and model simulations, and that we present here for the first time. Gravity wave forcing changes can have profound ramifications for the global climate, from polar vortex strength to ozone depletion and midlatitude weather.

KEYWORDS: Antarctica; Atmospheric circulation; Gravity waves; Climate variability; Orographic effects

1. Introduction

The static stability of the lower atmosphere in the polar regions is one of the highest on Earth. The surface atmosphere of West Antarctica and the Antarctic Peninsula has warmed at a rate of ≈0.3°–0.5°C decade^{-1}, equivalent to 1.5°–3°C since the 1950s depending on the exact time interval considered (Gonzalez and Fortuny 2018; Jones et al. 2019; Turner et al. 2020; Carrasco et al. 2021; Gorodetskaya et al. 2023; Bromwich et al. 2024). The observed warming is spatially heterogeneous, and especially pronounced in the northern part of the Peninsula, where early station records (e.g., Faraday–Vernadsky, Esperanza, and Rothera stations) indicate mean annual temperature increases of approximately 2°–3°C between the 1950s and late 1990s, followed by a period of cooling, or absence of warming, between 1999 and 2016. Recently, the warming trend has resumed, and, in February 2022, the Antarctic Peninsula has experienced a new extreme warm event with record-high surface temperatures (Gorodetskaya et al. 2023).

A surface atmosphere that warms up faster than the atmospheric layers above is expected to weaken atmospheric stratification and thus reduce static stability. Such changes in lower atmospheric stability can significantly influence the generation of orographic gravity waves (OGWs), which arise from the interaction between stably stratified flow and topography (Nappo 2013). Because of the high stability of the atmosphere, strong surface winds that often flow perpendicular to the ridge, and its steep topography, the Antarctic Peninsula is one of the most important sources of OGWs on the planet (Alexander et al. 2009; Hoffmann et al. 2013; Hindley et al. 2020). OGWs, also called "mountain waves," can propagate large distances horizontally (hundreds of kilometers away from the mountain

Denotes content that is immediately available upon publication as open access.

Supplemental information related to this paper is available at the Journals Online website: https://doi.org/10.1175/JCLI-D-25-0330.s1.

Corresponding author: Maria Vittoria Guarino, mariavittoria.guarino@enea.it

DOI: 10.1175/JCLI-D-25-0330.1

source) and vertically (up to ~120-km altitude) before eventually breaking.

The generation of OGWs is influenced by the flow regime near the surface. The type of flow regime is defined by the nondimensional mountain height $\hat{h} = Nh/U$ (also known as the inverse Froude number). This parameter takes into account, for hydrostatic mountain waves, the relative contributions of lower atmospheric stability as quantified by the Brunt–Väisälä frequency N, wind approaching the mountain U, and mountain height h in setting what portion of the incoming wind will flow over the mountain's top and what part of it will be blocked by the ridge or diverted around the mountain flanks.

A stable but less strongly stratified surface atmosphere promotes OGW generation (smaller $\hat{h}$) by allowing large-scale winds to flow over the mountain obstacle. This, in turn, weakens atmospheric blocking by the mountain at low levels (i.e., blocking drag). Generally, a flow-blocking regime refers to blocked flow conditions upstream of the mountain and a flow-over regime to gravity wave generation from the mountain.

Variations in upper-level OGW and low-level blocking drag on climate time scales can have major consequences for global climate (Sandu et al. 2016), from polar vortex strength to surface circulation. Near the surface, the type of flow regime over the Antarctic Peninsula influences the dynamics of Foehn winds (Elvidge et al. 2016), warm downslope winds whose frequency and intensity have been associated with surface ice-shelf melt (Marshall et al. 2006; King et al. 2017; Kirchgaessner et al. 2021). Flow-over regimes increase the ability of Foehn winds to descend at low levels and across the ice shelf (Elvidge et al. 2016). Thus, long-term changes in prevailing flow regimes can significantly impact surface mass and energy balance over the Peninsula with consequences for ice-shelf melt and stability.

In the upper layers of the atmosphere, trends in OGW forcing from Antarctica are key to predict and understand several aspects of atmosphere dynamics. Mountain waves produce an important drag force acting on the atmosphere and thus are a fundamental aspect of atmospheric circulation (Teixeira 2014). Weather and climate models with poor OGW representation suffer from significant troposphere and lower stratosphere biases, with incorrect representation of the Southern Hemisphere polar night jet and stratospheric temperatures (McLandress et al. 2012; Garcia et al. 2017). Gravity wave (GW) drag in the stratosphere plays a role in Antarctic stratospheric polar vortex breakdown in austral spring (Gupta et al. 2021), which has been linked to extreme weather events, including extreme heat and drought in Australia (Lim et al. 2019). Temperature fluctuations induced by mountain waves have also been shown to favor the formation of polar stratospheric clouds, which play a key role in the destruction phases of the ozone cycle (Dörnbrack et al. 2001; Höpfner et al. 2006; Orr et al. 2015). In the mesosphere and lower thermosphere, gravity waves that propagate above 80 km shape the chemical and dynamical structure of the upper atmosphere through momentum deposition and vertical transport of trace species (Eckermann et al. 2016; Guarino et al. 2024).

To date, implications of Antarctic surface warming on the stability of the atmosphere near the ground have not been formally investigated, and the consequences of changes in atmospheric stability for surface flow regimes in a warming climate are largely unknown.

Here, using a combination of latest-generation reanalysis data, in situ Antarctic station measurements, AIRS/*Aqua* satellite observations, and targeted simulations using the HadGEM3 global climate model, we investigate how Antarctic surface warming has impacted the stability of the lower atmosphere and what the implications are for gravity wave forcing from the Antarctic Peninsula.

2. Methods

a. *ERA5 reanalysis data*

We use the ECMWF ERA5 global reanalysis (Hersbach et al. 2020; Soci et al. 2024) from 1950 to 2022. ERA5 data are provided on a horizontal grid with 31-km resolution. Four-dimensional data were downloaded on pressure levels and interpolated on a geopotential height (GPH) vertical coordinate with equally spaced levels (Δz = 250 m). The high horizontal resolution allows a portion of the gravity wave spectrum to be explicitly resolved by ERA5, while the remaining part is parameterized by the Integrated Forecasting System (IFS) model using an OGW drag parameterization based on the Lott and Miller scheme (Lott and Miller 1997). The IFS model parameterizes the gravity wave and flow-blocking drag components using an approach that is similar to the one described below for HadGEM3 (Kanehama et al. 2022).

While satellite observations only became widely available for data assimilation in 1979, measurements of basic atmospheric properties over the Antarctic Peninsula actually started much earlier, and, in appendix B, we provide supporting analysis demonstrating the reliability of ERA5 reanalysis pre- and post-satellite era over the Antarctic Peninsula.

b. *HadGEM3 model simulations*

The numerical simulations presented here were performed using the HadGEM3-GC3.1-LL model, henceforth HadGEM3, developed by the U.K. Met Office (Williams et al. 2018; Kuhlbrodt et al. 2018). HadGEM3 is a fully coupled climate model that simulates the Earth System coupling the atmospheric Unified Model (UM; Walters et al. 2017), the land surface model JULES (Walters et al. 2017), the ocean model NEMO (Madec 2015), and the sea ice model CICE (Ridley et al. 2018). The model has a nominal horizontal resolution of ≈135 km for the atmosphere and ≈1° for the ocean. HadGEM3 uses 85 vertical levels (terrain-following hybrid height coordinate) from 0 to 85 km above the surface. We use historical simulations (four ensemble members, hereinafter referred to as "HIST"; Andrews et al. 2020) and a preindustrial control simulation (Menary et al. 2018) (hereinafter referred to as "PI") that were submitted to the Coupled Model Intercomparison Project phase 6 (CMIP6) (Eyring et al. 2016). The PI control simulation uses constant 1850 forcing, as prescribed by CMIP6 protocol, and was run for 500 years after spinup. The PI simulation provides the initial conditions for the historical simulations that simulate the global climate

from January 1850 until December 2014 using time varying (and occasionally spatially varying) forcings. All simulations use prescribed ozone concentrations. We analyze here the period from January 1950 to December 2014. For full details on model grid, settings, and on the analysis of the PI control and HIST simulations, please see Menary et al. (2018) and Andrews et al. (2020).

Two sensitivity experiments were performed to simulate flow-blocking (F_BLOCK) and flow-over (F_OVER) regimes. These simulations use the same historical forcings as HIST and were run from 1950 onward. At each time step, and within each grid cell, the model computes the Froude number $U/(Nh_{sso})$, where N is the Brunt–Väisälä frequency, U is the wind speed resolved in the direction of the low-level flow within a model-defined surface layer, and h_{sso} is the elevation of the model subgrid-scale orography (Walters et al. 2017). Different flow regimes were simulated by artificially increasing (decreasing) the h_{sso} for F_BLOCK (F_OVER). In the Unified Model orographic gravity wave drag parameterization, h_{sso} is proportional to the standard deviation of the mean orography within each grid box, σ, by a constant of proportionality called n_σ, so that $h_{sso} = n_\sigma\sigma$. The default value for n_σ in the UM model is 2.5. We changed n_σ to be 5 in the F_BLOCK simulation and 1.5 in the F_OVER simulation, with the modification applied only over Antarctica. Note that these changes to the mountain wave drag represent a significant doubling (for F_BLOCK) and almost halving (for F_OVER) of the subgrid mountain height, which was necessary to force flow regime transitions in the simulated Antarctic climate regardless of changes in wind or stability on seasonal and/or climate time scales.

We only altered the parameterized GW drag (and not the resolved component) because, in HadGEM3, GW drag from the Peninsula is mostly parameterized and the tip of the Peninsula, the largest contributor to mountain wave generation, is fully parameterized (see Fig. S1 in the online supplemental material).

c. AIRS satellite gravity wave observations

We use satellite observations of GW momentum fluxes (GWMF) from a climatology of AIRS/*Aqua* temperature measurements (Hoffmann and Alexander 2009; Hindley et al. 2020) covering the period from 2002 to 2024. AIRS is a hyperspectral near-infrared imager on board the *Aqua* satellite in a sun-synchronous orbit that provides measurements in a continuous 1780-km swath over the same location twice each day (Aumann et al. 2003). A specialized 3D temperature retrieval (Hoffmann and Alexander 2009) was developed for AIRS in which gravity wave perturbations can be measured throughout the stratosphere. These perturbations were then analyzed using 3D localized spectral analysis (Hindley et al. 2019) to develop the global climatology of zonal and meridional GWMF (Hindley et al. 2020) that we use here. The climatology was extended to 2024 for this study.

d. Data analysis

Spatial means are performed from [60°, 75°S] to [40°, 90°W] for the Antarctic Peninsula, unless otherwise specified. We look also at trends and time series for the wider West Antarctic region [60°, 90°S], [40°, 160°W]. The same geographical domains are used for HadGEM3 and ERA5. For HadGEM3, unless otherwise specified (e.g., for ensemble means) cross sections and maps for the historical simulations are always from ensemble member 1.

Trends in time series were tested for statistical significance using a modified Mann–Kendall trend test (Hamed and Rao 1998; Hussain and Mahmud 2019), suitable for climate data that often exhibit some degree of autocorrelation. To estimate trends, we used the Theil–Sen's slope estimator method that is robust against outliers in time series (Theil 1950; Sen 1968). Anomaly fields were tested for statistical significance using a two-sided Welch's t test. For scatterplots, we used linear regression analysis to estimate slope and statistical significance (Virtanen et al. 2020).

1) Static stability and Nh/U

To compute the Brunt–Väisälä frequency N, we used the following gradient formula for N^2:

$$N^2 = \frac{g}{\theta}\frac{\partial\theta}{\partial z}, \tag{1}$$

where g is the acceleration due to gravity, θ is the potential temperature, and z is the vertical coordinate. For ERA5, z is a geopotential height vertical coordinate; for HadGEM3, we use height-above-the-surface vertical levels. We used monthly means for θ and central finite differences to compute (1). We averaged the resulting N over land points only (see below).

To assess flow regime changes, we complement our analysis with nondimensional mountain height $\hat{h} = Nh/U$ estimates. Studies based on linear gravity wave theory and idealized model simulations have shown that typically, for 3D mountains, $\hat{h}$ values between 1.5 and 2 mark a transition point across two flow regimes (Smith 1980, 1989; Miranda and James 1992), with the amplitude of the excited waves expected to be largest for $\hat{h} \approx 1$. Using this simple nondimensional parameter in real-world applications poses some challenges (Reinecke and Durran 2008); $\hat{h}$ is a predictor of flow-blocking/flow-over conditions based on the linear theory of frictionless airflow over a single isolated mountain embedded in a background flow in which both wind speed and static stability are constant upstream and on top of the mountain. The value of $\hat{h}$ should be calculated using the speed of the wind approaching the top of the mountain (cross-barrier wind) and the static stability near the top of the mountain for each mountain peak. However, the presence of a boundary layer, and variations in wind and static stability with height upstream and/or above the mountain, can change the flow behavior in terms of surface blocking and gravity wave amplitude with respect to linear theory predictions.

For the purposes of this study, we are interested in the mean-flow behavior over a large area (i.e., the Antarctic Peninsula) with prominent orographic features that span across several degrees in latitudes and longitudes. For example, the most northern part of the Peninsula (north of 68°S) extends from 66° to 58°W meaning that the definitions of "upstream" or "cross barrier" are not universal. Here, $\hat{h}$ calculations are

carried out at each grid point using monthly means of the wind speed U at 10 m and monthly means of N averaged over the lowest 1 km of the atmosphere above the orography. We use the lowest 1 km of the atmosphere because this height range includes the full depth of the polar shallow boundary layer, which can vary from a few tens to a few hundreds of meters, and this is where we find the strongest N trends (see section 3a). This approach of computing $\hat{h}$ is analog to the IFS and UM model parameterizations in which Froude number computations are carried out separately for each grid cell (see section 2b). The $\hat{h}$ calculations are carried out only for surface elevations greater than 100 m ($h \geq 100$ m). To obtain time series of $\hat{h}$ over the Peninsula, we first compute 2D maps and then spatially average them using the geographical boundaries specified above.

Note that the computation of $\hat{h}$ is sensitive to temporal averaging. For example, using instantaneous value of N and U to compute monthly means of Nh/U would yield higher values than those presented here (Simmonds and Lim 2009). However, a comparison between $\hat{h}$ time series derived from 6-hourly data and those based on monthly means over a 20-yr period shows that the two differ primarily in magnitude (with the 6-hourly estimates being about 30% higher), while their variability, trends, and overall behavior remain unchanged (not shown). Given our focus on the relative roles of surface wind and stability in shaping flow behavior and how this might change over time, monthly means provide a reliable and computationally efficient basis for this analysis.

2) Gravity wave forcing proxies

To quantify parameterized GW activity in HadGEM3 and ERA5, we use variables directly available from model outputs. For HadGEM3 simulations, we analyze the absolute GW saturation stress, which is a measure of wave breaking, averaged through the lowest 10 km of the atmosphere. This stress represents the force per unit area exerted by breaking waves on the atmosphere. For ERA5 parameterized waves, we use the GW dissipation term vertically integrated throughout the entire column; this is also a measure of wave breaking. This parameter is the amount of energy per unit area that is converted into heat when orographic gravity waves break.

To quantify ERA5 resolved wave activity, we use the vertical velocity temporal variance at 500 hPa Var(ω) (midtroposphere, at $\approx$5 km above the surface), which gives us an estimate of how many (or what amplitude) GWs are generated from the Peninsula. To compute Var(ω), we used ERA5 vertical velocity ω (Pa s^{-1}) data at 6-hourly frequency. Computations were carried out on selected pressure levels and for a narrow region surrounding the Peninsula. The input ω field was filtered in Fourier space to isolate mountain waves and remove wavenumbers outside of the expected range. See appendix A for further details.

GW activity from observations was assessed using satellite-derived GWMF; momentum fluxes also inform us on the number and/or the amplitude of waves propagating in the atmosphere. To compute the GWMF trends, we calculated the net zonal GWMF between 30 and 42 km over the region shown in Fig. A1 for each month so that randomly orientated fluctuations due to instrument and/or retrieval noise cancel to zero. This means that our trends are robust to changes in instrument noise over time. Trends were fitted to each month for all years through 2002–24 (i.e., all Januarys, all Februarys, all Marches, and so on). To obtain confidence statistics on these trends, a bootstrapping approach was applied. For each monthly time series, instead of applying a linear fit to all 23 years, we create a time series using data from randomly sampled years 23 times, allowing for the same year to be selected more than once (known as replacement). If a year is selected multiple times, it is given a weighting greater than 1, after which all weights are normalized so that they sum to 1. We then perform a weighted linear fit using these weightings. This process is repeated 500 times for each monthly time series, producing a broad distribution of fitted trends.

3. Results

a. Atmospheric stability

ERA5 reanalysis shows that in the lowest 1 km of the atmosphere over the Antarctic Peninsula, the Brunt–Väisälä frequency has been steadily decreasing since 1950 (Fig. 1). This means that the lowest atmospheric layers can more easily mix with the layers above, and that the polar surface atmosphere has become less strongly stratified and, thus, less stable.

The decrease in atmospheric stability is driven by surface warming: in Figs. 2a and 2b, the pattern of surface warming is mirrored by the stability decrease. ERA5 annual-mean surface air temperature (SAT) trends are $\approx$+0.5° to +0.75°C decade^{-1} for the Peninsula (Fig. 2a), with larger trends occurring on seasonal basis. Enhanced surface heat fluxes due to warming lead to increased atmospheric mixing, reducing stability.

ERA5 shows that the bottom 1 km N over the Peninsula has undergone a clear shift: annual means of N in Fig. 1 are consistently above the 1950–2022 mean (solid thin line) for the period $\approx$ 1950–90 (red shades) and begin declining afterward. From 1990 to 2022, annual means of N remain mostly well below the long-term mean (gray shades). Negative trends in N are strongest near the surface (where atmospheric warming is the largest) and weaken with the altitude (Fig. 2c). In general, negative trends in N are observed in the lowest 1–3 km above the ground in all seasons. A similar behavior is simulated by the HadGEM3 model. During the historical period, HadGEM3 simulates a steady decline in N in the lowest 1 km of the atmosphere in all seasons but summer (DJF) (Fig. 3), during which HadGEM3 SAT trends for the Peninsula and West Antarctica are nearly zero (Figs. S6 and S7).

Both the model and reanalysis show consistent changes regarding the thermal structure and stability of the lower atmosphere. Therefore, we next explore how historical trends in N compare with those arising from natural climate variability using the HadGEM3 PI control simulation. To this end, we analyzed the Antarctic Peninsula and the broader West Antarctic region separately and found similar behavior in both. Here, we present results for the wider West Antarctic

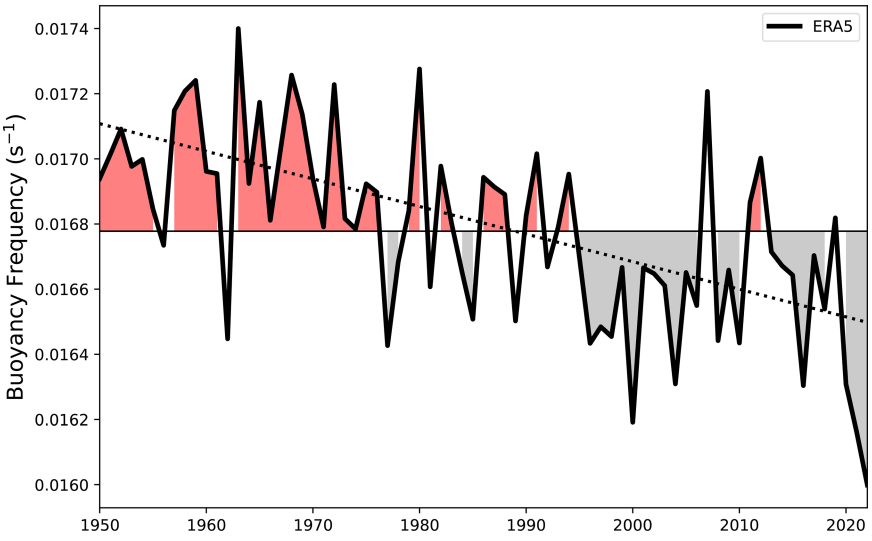

FIG. 1. Time series of the annual Brunt–Väisälä frequency for the lowest 1 km of the atmosphere over the Antarctic Peninsula (land points only) from ERA5. The solid thin line is the long-term mean, and shaded areas represent values above (red) and below (gray) the mean. The slope of the regression line (dotted line) is statistically significant ($p < 0.01$).

region (see also appendix B), while corresponding trends for the narrower region of the Antarctic Peninsula are shown in Fig. S8. The trends and variability of the broader West Antarctic region provide a more robust assessment of long-term changes by capturing the influence of large-scale circulation patterns that extend beyond the Peninsula (such as the Amundsen Sea low and polar jet variability), offering a more representative view of regional climate variability.

Although the atmosphere in HadGEM3 is on average more strongly stratified (larger N), negative N trends for West Antarctica are of the same order of magnitude in HadGEM3 and ERA5 (Fig. 3). ERA5 trends (stars in Fig. 3) are rather consistent throughout the seasons and are always closer to -1×10^{-4} Hz decade^{-1}. HadGEM3 ensemble members simulate N trends mostly within the -5×10^{-5} to -1×10^{-4} Hz decade^{-1} interval for all seasons (orange diamonds in Fig. 3), except DJF (see above). HadGEM3 ensemble means have the strongest negative trends in spring (SON) and autumn (MAM) (red hexagons in Figs. 3b,d), i.e., when the largest SAT warming trends occur over the Peninsula (Fig. S7). Under 500 years of constant preindustrial forcing (blue circles in Fig. 3), HadGEM3 never produces trends over a 65-yr period comparable to those found in the historical simulations (apart from the summer season and one ensemble member in JJA). PI trends are both positive and negative and mostly spread around zero. ERA5 N trends (computed over 70 years from 1950 to 2022) are always outside the expected range of natural climate variability as simulated by HadGEM3.

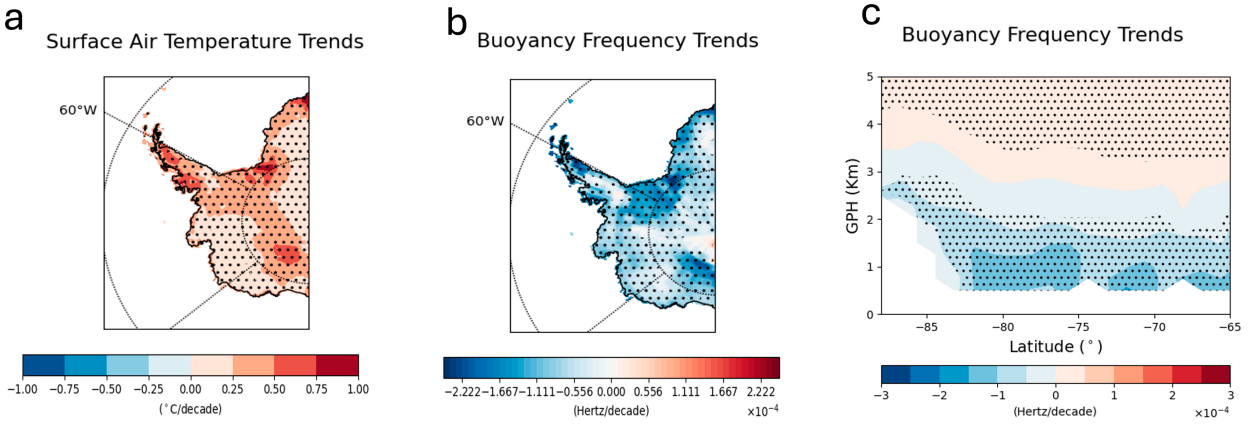

FIG. 2. (a) ERA5 SAT and (b) lowest 1-km N trends over land from 1950 to 2022. (c) ERA5 zonal mean N trends from 65° to 90°S through the lowest 5 km of the atmosphere over the Antarctic Peninsula ([40°, 90°W]), land points only, from 1950 to 2022. Data points are masked only when all grid points in the zonal mean are masked, thus showing main orographic features. Dots indicate statistical significance at 95%.

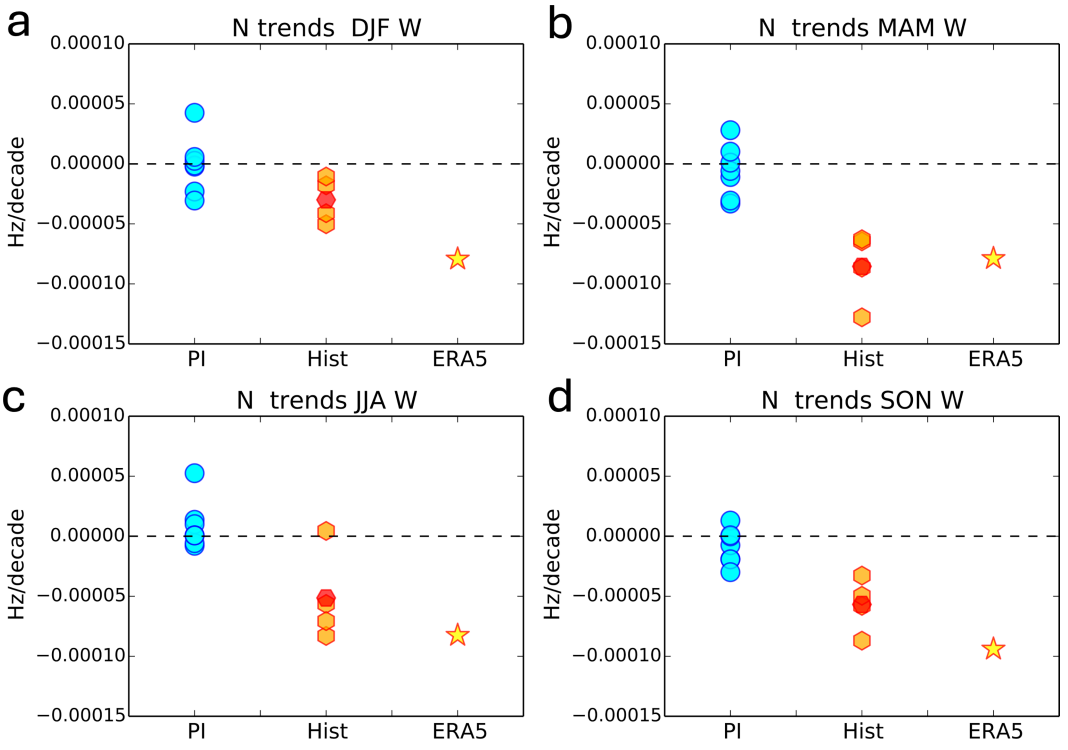

FIG. 3. Lowest 1-km Brunt–Väisälä frequency trends over West Antarctica for the HadGEM3 PI control simulation (blue circles), the four historical ensemble members (orange diamonds; the red hexagon is the ensemble mean), and ERA5 reanalysis (star). For the PI control run, circles represent trends computed over 65 years each.

b. Flow regimes

In principle, the decrease in static stability discussed above could alter the generation of mountain waves from the Antarctic Peninsula by modifying the surface flow regime. OGW generation does not depend only on N but rather on the balance between buoyancy forces and winds as quantified by the nondimensional mountain height $\hat{h} = Nh/U$.

In ERA5, $\hat{h}$ computed over the Antarctic Peninsula decreases with time in all seasons (Fig. 4d). To illustrate what a regional decrease in $\hat{h}$ looks like, we show maps of $\hat{h}$ for two cases: September 1952 (Fig. 4a), September 2021 (Fig. 4b), and their difference (Fig. 4c). At the beginning of the historical period (Fig. 4a), the ridge of the whole mountain range extending from ≈75°S to the tip of the Peninsula near 63°S shows large $\hat{h}$ values (red colors). This indicates that the flow impinging on the mountain range is blocked upstream and only partially able to rise over the mountains. Mean atmospheric conditions for the same month but toward the end of the historical period, in 2021, are different: estimates of $\hat{h}$ over the mountain ridge have decreased in several locations, thus a larger portion of the flow is allowed to pass over the mountain. The respective N and U fields used to compute the maps shown in Figs. 4a–c are shown in Fig. S9.

The statistically significant decline in $\hat{h}$ over the historical period points to a shift in the prevailing flow regime for which gravity wave generation is favored over time. A negative trend in $\hat{h}$ signifies a reduction of the depth of the blocked layer (the lowermost part of the flow approaching the mountain) and thus an increase in the effective mountain height (i.e., the height of the mountain above the blocked layer), which determines the gravity wave amplitude and thus GW drag.

Figure 5 shows seasonal time series of $\hat{h}$ and gravity wave dissipation term. For both quantities, we show anomalies computed against the long-term mean and normalized with respect their absolute maximum, so that both variables take values between −1 and 1. We can see that $\hat{h}$ and the GW dissipation term are strongly anticorrelated, clearly showing that the generation of gravity waves in ERA5 responds to surface flow regime changes as diagnosed by our $\hat{h}$ estimates. Particularly, lower values of $\hat{h}$ (blue lines in Fig. 5) correspond to more intense dissipation of gravity waves (yellow lines in Fig. 5) throughout the atmospheric column, implying a larger production at the source.

DRIVERS OF FLOW REGIME CHANGES

Since both changes in surface static stability and wind speed can contribute to change $\hat{h}$, it is important to look at what process might be mainly responsible for the observed trends, although fully separating the two is not possible given the existence of complex feedbacks between wind and stability.

Similarly to a weaker static stability, a stronger wind can favor gravity wave generation. However, unlike N trends, which are negative and statistically significant in all seasons (Fig. 3 and Fig. S4), for U (wind speed at 10 m), we find significant positive

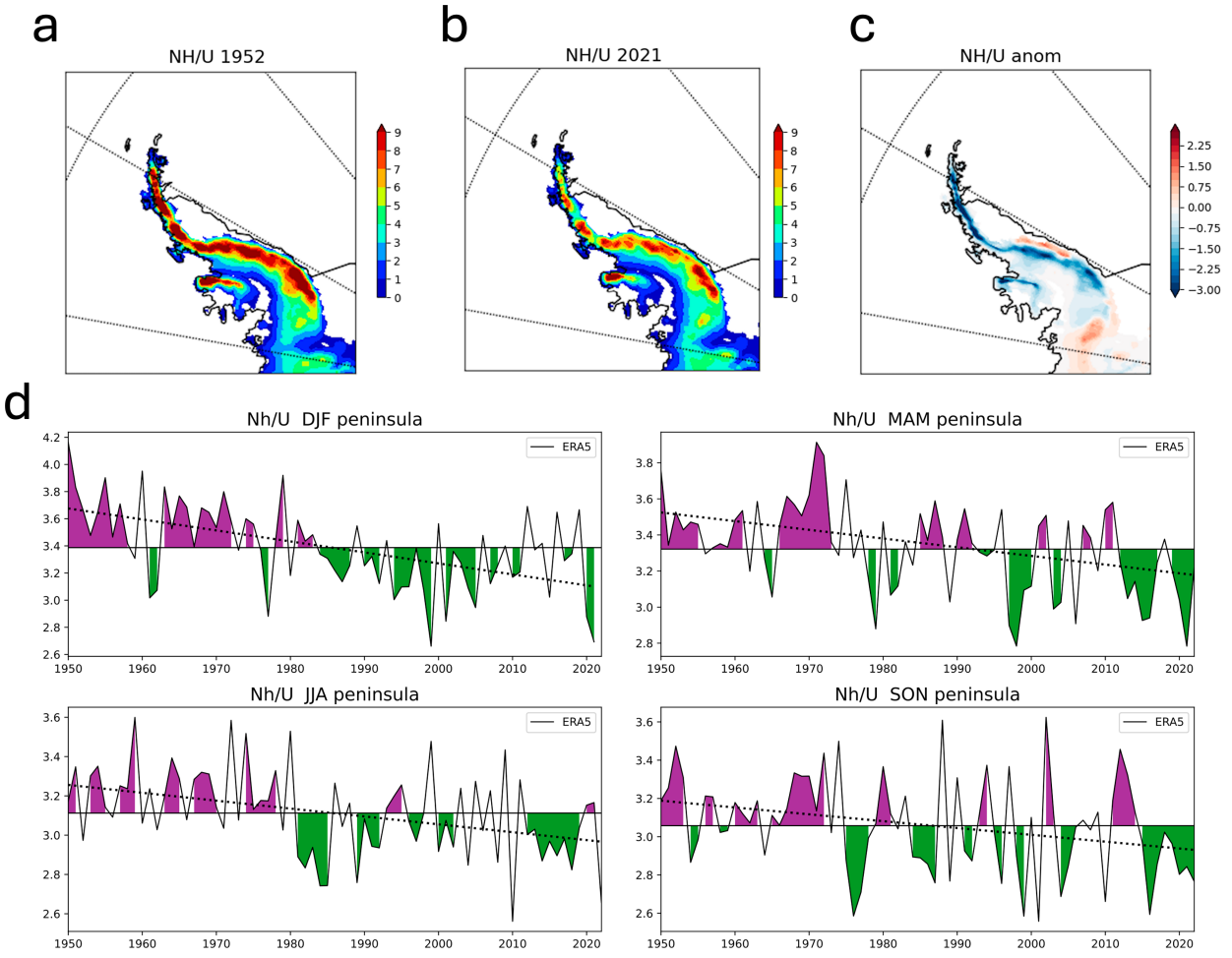

FIG. 4. ERA5 $\hat{h} = Nh/U$ maps for (a) September 1952, (b) September 2021, and (c) their 2021–1952 difference. (d) Time series of $\hat{h}$ for each season averaged over the Antarctic Peninsula. The solid thin line is the long-term mean, and shaded areas represent values above (purple) and below (green) the mean. The slope of the regression line (dotted line) is statistically significant for all seasons ($p < 0.01$).

trends for DJF and MAM only (Fig. 6). This result is in agreement with previous studies (e.g., Simmonds and Li 2021). Therefore, N trends are the most likely driver of the decrease in $\hat{h}$ detected in all seasons (Fig. 4).

The trends in U discussed above refer to the speed of the flow over land used for $\hat{h}$ calculations. However, trends over land can be difficult to interpret because of an interdependency between wind and static stability: on the one hand, a weaker stability can increase the wind speed over the mountain's top by allowing a larger portion of the flow to rise over it; on the other hand, a stronger wind can decrease stability by increasing turbulent mixing in the boundary layer. An attempt to disentangle these processes can be made by looking at (far) upstream conditions. We computed time series for the westerlies (zonal wind component $u > 0$ only) at 10 m averaged over a box located in the Bellingshausen Sea; we picked a region that is well upstream of the Peninsula ([60°–68°S, 74°–100°W], Fig. 6f) to limit further feedbacks on the wind speed in the proximity of the mountains that could derive from changes in upstream blocking over time. We looked at westerlies only because, besides being the crosswind component relative to the Peninsula, an increase/decrease of the surface wind speed in this region can be linked to changes in the v component associated with the variability of the Amundsen Sea low, and so to the north–south circulation in the basin. Unlike wind speed over land that increases in DJF and MAM, we find that upstream wind conditions show statistically significant trends only for DJF and SON (Fig. 6). This confirms, for summer, an important role of large-scale winds in setting the surface wind (and thus the flow regime, see section 3c), and for all other seasons, that a combination of large-scale circulation forcing and N trends influences the surface wind field over the Peninsula. For MAM, in particular (Figs. 6b,f), upstream winds do not strengthen during the historical period, but the positive trend in U over land might be the result of the strong decrease in N for that season (Fig. S4).

Regarding the possibility that stronger winds decrease stability, from the analysis above it is clear that N trends are independent of wind trends (upstream and over land) for at least two out of four seasons. This confirms that N trends

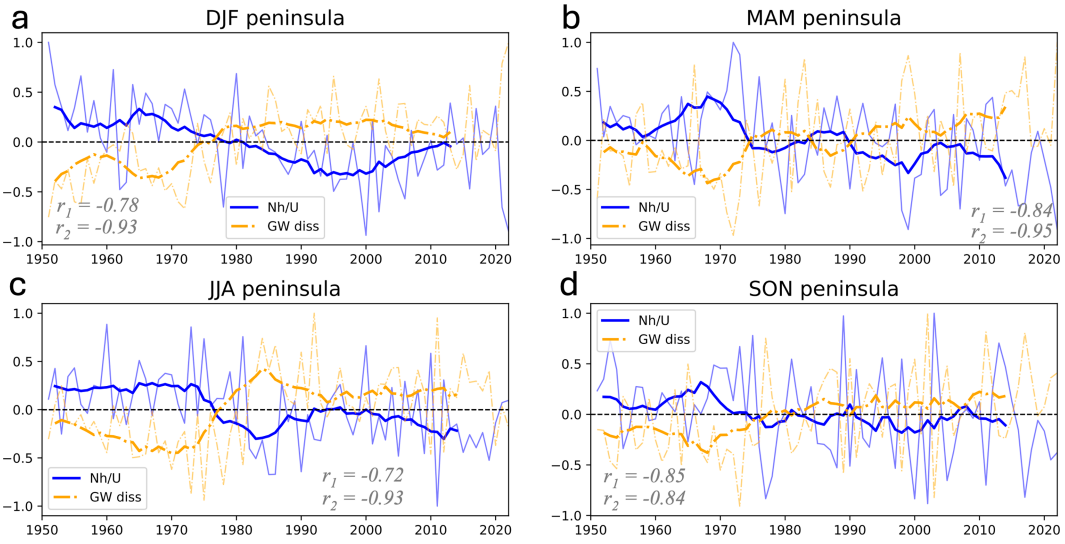

FIG. 5. Seasonal time series of ERA5 $\hat{h} = Nh/U$ and the GW dissipation term averaged over the Antarctic Peninsula (normalized anomalies against the mean). Thin lines are annual means, and thick lines are 10-yr running means. Pearson correlation coefficients for the annual mean (r_1) and 10-yr running mean time series (r_2) are also shown.

must be primarily driven by surface warming, as discussed in section 3a. Further confirmation on this comes from HadGEM3. As mentioned above, N decreases in the model in all seasons but summer. The summer season is, however, the only one in which HadGEM3 10-m wind speed over the Peninsula has a strong and statistically significant trend, while in all other seasons, the model shows no trends (Fig. S10). We therefore exclude a prominent role of surface winds in driving N trends.

c. *Gravity wave forcing*

In response to a decreasing N, increasing GW trends are detected in ERA5 reanalysis (Figs. 7a,b), AIRS/*Aqua* satellite observations (Fig. 7c), and HadGEM3 model simulations (circles in Fig. 8a).

When the ERA5 annual GW dissipation term and vertical velocity variance Var(ω) at 500hPa are plotted against the lowest 1-km N over the Peninsula (Figs. 7a,b), the two quantities exhibit a negative correlation. Pearson correlation coefficients are −0.5 and −0.6, respectively. A clear temporal transition is seen for these variables: ERA5 shows a shift from a high-N/low-GW forcing state at the beginning of the historical period (purple colors) to a low-N/high-GW forcing state toward the end of the historical period (green colors).

This transition in GW forcing is simulated by HadGEM3 too. In Fig. 8a, the model annual GW stress (circles) varies with N in a similar fashion (correlation: −0.6). A shift in the mean properties of these variables over time indicates a less stable atmosphere over the Antarctic Peninsula and a stronger generation of OGWs from the mountain source beneath.

Besides annual means, shown here, we also studied the flow behavior at the seasonal level (figures shown in supplemental, Figs. S6 and S11–S12) and found that GW forcing changes are coherent with N changes in all seasons. In ERA5, GW dissipation term increases in all seasons when N decreases (Fig. S11). In HadGEM3, when N strongly decreases in the model (in SON and MAM) (Fig. S6), trends in GW saturation stress are positive and statistically significant (Fig. S12). The DJF increase in GW forcing in the model is, however, driven solely by increasing westerlies (Fig. S10) (see section 3b for further discussion on this) since summertime N does not decrease in HadGEM3.

The ERA5 and HadGEM3 increase in DJF surface winds is due to the summertime positive trend in the Southern Annular Mode (SAM), which has been largely attributed to stratospheric ozone depletion (Thompson and Solomon 2002; Arblaster and Meehl 2006), and the associated poleward shift of the westerlies (Deng et al. 2022). Because of this, stronger winds blow over the Peninsula and favor the generation of gravity waves. A similar result was found by Orr et al. (2008), who studied the flow behavior over the Peninsula in response to the westerly flow intensification in summer. Therefore, we conclude that, for summer only, the increased GW forcing is driven by both a decrease in static stability and an increase in surface winds; for all other seasons, the weakening static stability has a leading-order effect in driving a flow regime shift and increasing GW forcing from the Peninsula.

Supporting our thesis of a shift in flow regimes are satellite observations of gravity wave momentum fluxes. In Fig. 7c, we show mean trends for GWMF derived from AIRS/*Aqua* satellite observations (dark pink dots) and 50% and 95% confidence intervals (pink bars) of the trend distributions for each month (see methods). Observed GWMF shows increasing trends in stratospheric GW activity during winter and spring, when mountain waves can propagate to the stratosphere. This independent observational result supports our hypothesis of increased GW forcing from the Peninsula as a result of decreasing stability. We acknowledge, however, that long-term changes in wind filtering can also modulate the observed

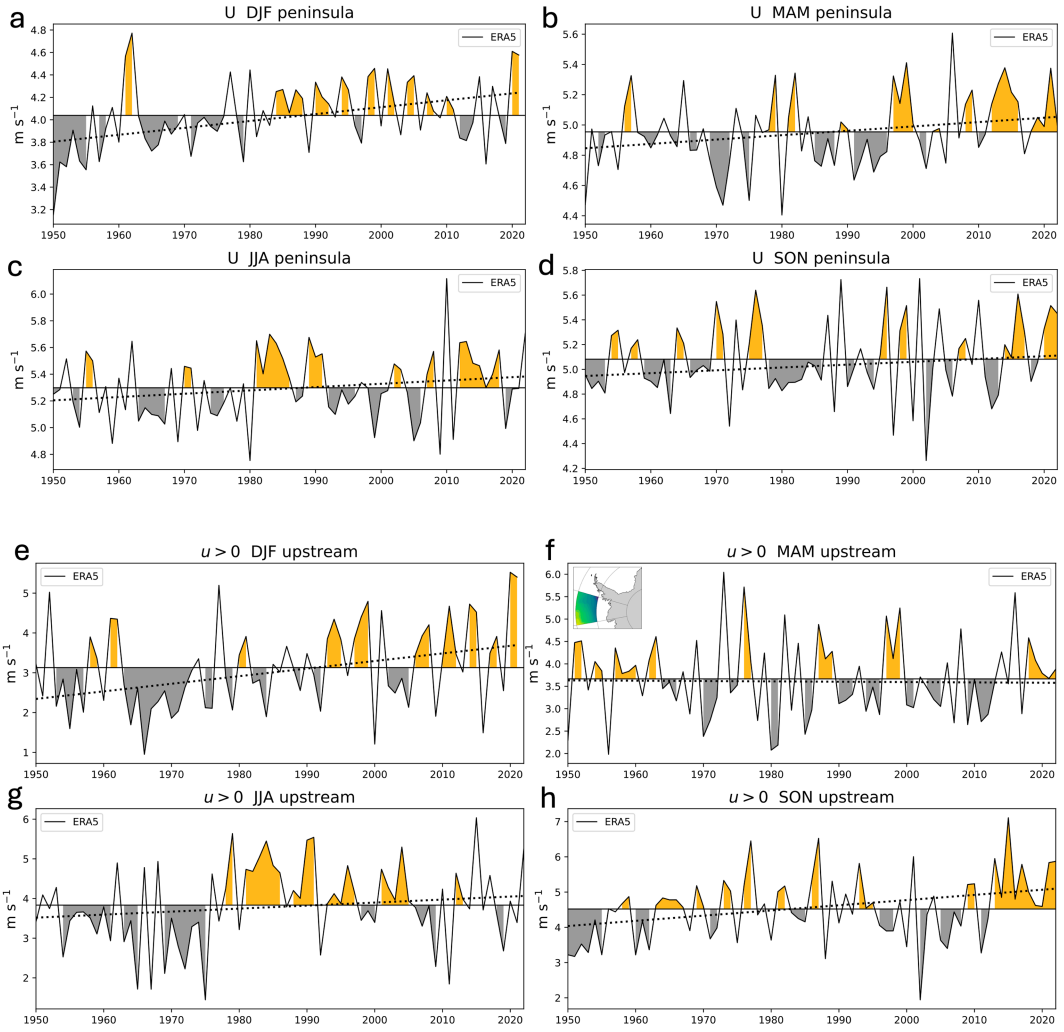

FIG. 6. (a)–(d) Seasonal time series of ERA5 wind speed at 10 m over land (U) averaged over the Antarctic Peninsula used for $\hat{h}$ calculations. The solid thin line is the long-term mean, and shaded areas represent values above (orange) and below (gray) the mean. The slope of the regression line (dotted line) is statistically significant for DJF and MAM ($p < 0.01$) and not statistically significant ($p > 0.05$) for JJA and SON. (e)–(h) Zonal wind component ($u > 0$ only) at 10 m averaged over a box ([60°–68°S, 74°–100°W]) upstream of the Antarctic Peninsula shown in (f). The slope of the regression line (dotted line) is statistically significant ($p < 0.01$) for DJF and SON and nonstatistically significant for MAM and JJA ($p > 0.05$).

GWMF reaching the stratosphere (which will be explored in a future study), but the results shown here are consistent with our hypothesis. These trends are also not affected by changes in instrument noise because we use the average net zonal momentum flux, for which randomly orientated fluctuations due to noise in the AIRS measurements average to zero.

d. *From flow blocking to flow over*

To test the hypothesis of a flow regime shift during the historical period, we performed two sensitivity experiments in which the climate system in HadGEM3 is forced under a perennial state of flow-blocking (F_BLOCK simulation) and flow-over (F_OVER simulation) conditions. This means that, independently of the embedded climate change signal, the flow is always mostly blocked in F_BLOCK and mostly able to flow over the mountain's top in F_OVER.

In F_BLOCK, low-level blocking is large, and GW saturation stress (pentagons in Fig. 8a) is lower than the historical simulation ensemble mean (HIST, circles in Fig. 8a). The tropospheric polar vortex is stronger in F_BLOCK (Fig. 8b) because of the weaker GW forcing. On the contrary, in F_OVER, GW production is favored, and the saturation stress is always larger than HIST (hexagons in Fig. 8a). Enhanced gravity wave breaking in F_OVER weakens the polar vortex by decelerating the background flow to a greater extent (Fig. 8c). Under the two scenarios of a much stronger (weaker) polar vortex, the Antarctic continent becomes much colder (warmer) in F_BLOCK (F_OVER) (not shown). Thus,

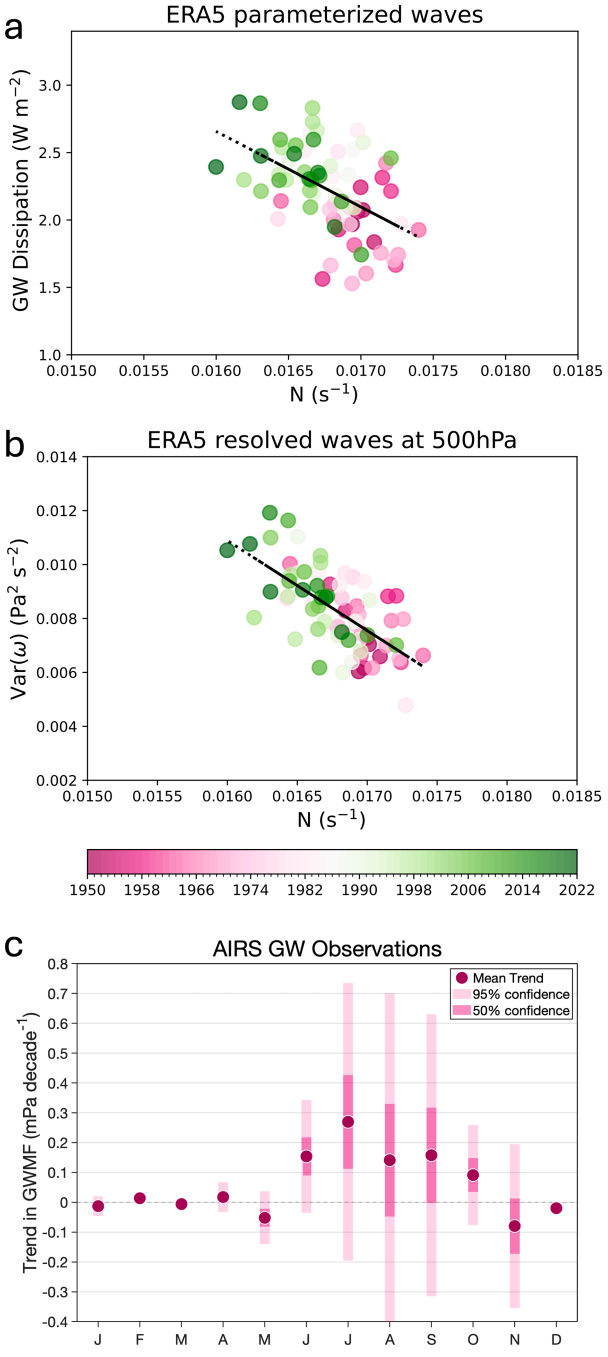

FIG. 7. (a) GW dissipation term (W m^{-2}) for parameterized waves and (b) vertical velocity variance Var(ω) (Pa^2 s^{-1}) of resolved gravity waves vs N (s^{-1}) from ERA5. Color bar represents time from 1950 to 2022. All values are annual means and averaged over the Antarctic Peninsula. The solid black lines in (a) and (b) are the regression lines ($p < 0.01$). (c) Monthly trends in net stratospheric GWMF from AIRS/*Aqua* satellite observations over the Antarctic Peninsula from 2002 to 2024. Dots indicate bootstrapped-mean trends, and 50% and 95% confidence intervals are shown by pink and dark pink bars, respectively.

our sensitivity experiments represent two opposite scenarios: a very cold (warm) Antarctic climate with high (low) atmospheric stability at the ground and weaker (stronger) GW forcing. The ensemble mean of the HadGEM3 historical simulations lies between these two scenarios and appears to be transitioning from one state to the other with time (color bar in Fig. 8a). In the regime diagram of Fig. 8a, HIST (circles) is closer to flow-blocking conditions (pentagons) at the beginning of the historical period and to flow-over conditions (hexagons) by the end. This corroborates the temporal transition observed in ERA5 and simulated by HadGEM3, for which GW forcing from the Antarctic Peninsula has shifted from a flow-blocking to a flow-over regime type since 1950.

Note that, while during the historical period, the shift in flow regimes discussed in this study is promoted by a decreasing N, in the two sensitivity experiments we change Nh_{sso}/U by varying h_{sso}. This approach is justified since it is the actual value of $\hat{h}$ that defines the flow behavior at the surface, regardless of which of the three variables (N, h, U) has been varied.

4. Discussion and conclusions

a. *Other mechanisms for GW forcing changes*

Besides variations in $\hat{h}$, there exist other mechanisms, such as variations of wind and/or stability with height in the free troposphere, that can influence where and how gravity waves force the atmosphere. Both ERA5 and HadGEM3 simulate tropospheric warming (≈0–10 km above the surface) and stratospheric cooling (≈20–25 km above the surface) during the historical period (Gulev et al. 2021), which affect atmospheric static stability by decreasing it in the troposphere and increasing in the stratosphere (Figs. S13 and S14). For waves that are near saturation (i.e., about to break), the decrease/increase of N with height should, in principle, discourage gravity wave breaking in the lower layers of the atmosphere and favor it in the layers above, according to enhanced saturation theory (VanZandt and Fritts 1989). Despite the decrease in tropospheric static stability, we find an increase in HadGEM3 GW saturation stress within the lowest 10 km of the atmosphere and an increase in the production of ERA5 resolved waves in the troposphere. Furthermore, the ERA5 GW dissipation term, which accounts for parameterized OGWs breaking everywhere in the vertical column, has a positive trend, implying a net increase in gravity wave breaking. Note that a simple upward shift of where the GW forcing is exerted should not result in any significant trend. All of the above indicates that the observed changes in gravity wave forcing must be driven by flow regime changes at the surface.

Confirmation of increasing GW activity in the Antarctic stratosphere is provided by AIRS satellite–derived momentum fluxes. Note that because a similar long-term climatology for gravity waves in the troposphere does not exist, model simulations and reanalyses are the only means we have to assess tropospheric changes in GW forcing to date.

Trends in large-scale climate indices, such as the SAM, which can modulate wind speeds and wind shear through the

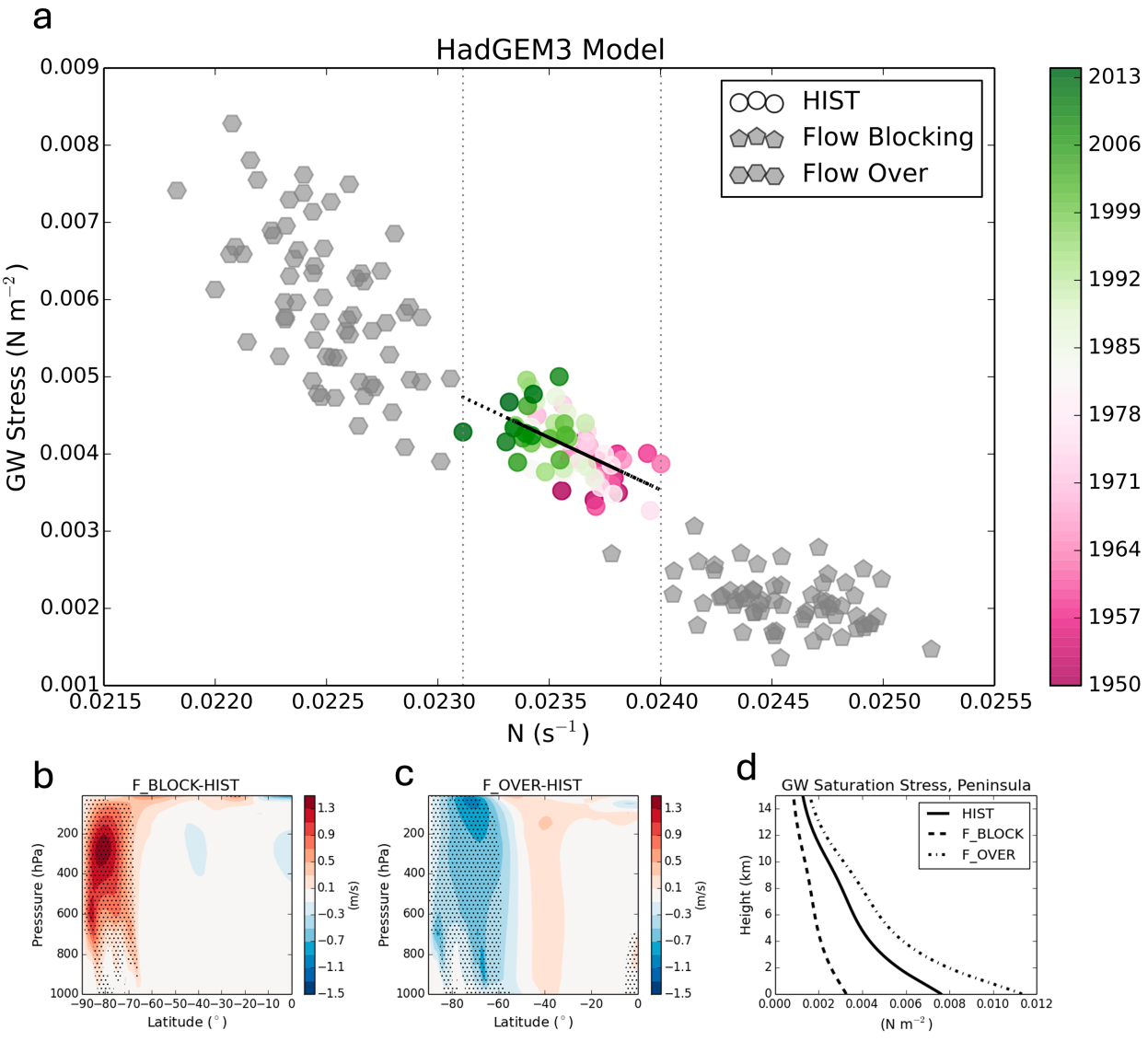

FIG. 8. (a) Ensemble mean of the absolute gravity wave saturation stress GW Stress (N m^{-2}) vs the lowest 1-km Brunt–Väisälä frequency N (s^{-1}) over the Antarctic Peninsula as simulated by the HadGEM3 model during the historical period (HIST; circles). Dashed vertical lines mark the maximum and minimum values for HIST. Color bar represents time from 1950 to 2014. The flow-blocking (F_BLOCK; pentagons) and flow-over (F_OVER; hexagons) simulations are shown in gray. All values are annual means. The solid black line is the regression line ($p < 0.01$). (b) F_BLOCK-HIST and (c) F_OVER-HIST Southern Hemisphere zonal-mean zonal wind anomalies (m s^{-1}). Dots indicate statistical significance at 95%. (d) Vertical profiles of the absolute gravity wave saturation stress averaged over the Antarctic Peninsula for HIST (solid line), F_BLOCK (dashed line), and F_OVER (dash–dotted line). All quantities are annual means.

troposphere, could also impact gravity wave forcing by altering the presence and altitudes of critical levels (Smith 1977; Guarino et al. 2016). However, the positive trend in the SAM since the mid-1960s is actually largest during the summer and autumn months (Thompson and Solomon 2002; Simmonds 2015), when gravity wave generation is weaker, so this does not conflict with our hypothesis.

b. *Implications of a shift in prevailing flow regime*

We consider now possible implications of a shift in the prevailing flow regime over the Antarctic Peninsula.

For summer, the increase in GW forcing was found to be driven mostly by a positive trend in the westerlies. GW drag is weakest in summer, and, because of the stratospheric wind reversal from westerly to easterly, OGWs cannot propagate into the stratosphere during DJF (Fig. 7c) so changes in summertime GW forcing are likely to be of less significance. On the contrary, a sustained trend in GW forcing in austral spring is important for the dynamics of the stratospheric polar vortex and the timing of its breakdown (Gupta et al. 2021). Model and reanalyses both agree on positive trends in GW forcing during austral spring and autumn driven by large N

negative trends. Breaking GWs in the stratosphere weaken the polar vortex, which has broader implications since Southern Hemisphere polar vortex weakening has been linked to extreme weather at midlatitudes (Lim et al. 2019) and is important to ozone chemistry and the prediction of the southern polar ozone hole.

Regardless of the season, more (or larger amplitude) OGWs that break in the troposphere mean a greater deceleration of the background flow, which leads to a weaker tropospheric polar vortex. This slows down the polar-front jet stream and thus the westerlies at the ground (Fig. 8c). In this respect, one could think of the positive trend in the GW forcing presented here as an antagonist process to the observed trend in the SAM. Disentangling the two processes on climatic time scales would be of great importance.

Surface flow regime changes can modulate the occurrence and dynamics of Foehn winds across the Antarctic Peninsula. Marshall et al. (2006) associated the increased surface melt that led to the loss of the Larsen A and B ice shelves in 1995 and 2002 to an increased frequency of Foehn events driven by the positive trend in the summer westerlies. Different flow regimes have been shown to modify the pattern and magnitude of surface warming over the Larsen C ice shelf associated with Foehn events (King et al. 2017; Kirchgaessner et al. 2021). Compared to blocked-flow conditions that limit the effective mountain height, in a flow-over regime, the flow is able to ascend and descend across a larger portion of the mountain. Foehn winds during flow-over conditions lead to an increase in upwind precipitation because the air is sourced from lower moisture-rich regions, and deliver larger fluxes of sensible heat to the ice shelf (Elvidge et al. 2016). By making flow-over regime conditions more likely, the long-term shift in flow regimes described here should, in principle, contribute to increasing upwind precipitation and downwind surface warming with consequences for the Larsen C ice-shelf melt.

While we looked at vertically propagating gravity waves, an increase in the frequency of flow-over conditions can affect directly the occurrence of trapped gravity waves, a type of gravity waves that is trapped at low levels and propagates far downstream of the mountain. Trapped gravity wave drag at low levels plays a crucial role in modulating the intensity of Antarctic surface winds, which, in coastal regions, are important for the opening of coastal polynyas and thus sea ice formation (Vignon et al. 2020).

Finally, although this work focused on assessing changes in GW drag, a shift in prevailing flow regime over the Antarctic Peninsula is expected to have important consequences for the low-level blocking drag and thus the Antarctic surface circulation. As N decreases over time, and blocked-flow conditions become less frequent, the low-level blocking drag weakens accordingly. If blocking from the Antarctic Peninsula (which manifests itself as a positive mean sea level pressure anomaly) lessens significantly, changes in the pressure and thus wind fields on the windward (Bellingshausen and Amundsen Seas) and lee (Weddell Sea) sides of the mountains should be expected. Ultimately, this could lead to significant alteration in ocean–ice–atmosphere coupling in these regions, which are renowned sites of Antarctic Bottom Water formation and sea ice production and export. Consequences of changing flow regimes for surface and regional circulation changes remain a topic for future investigation.

To conclude, in this study, we have shown that the surface atmosphere over the Antarctic Peninsula has become less stable since the 1950s. Changes in the lowest 1-km Brunt–Väisälä frequency have consequences for gravity wave forcing from Antarctica. In response to a decreasing Brunt–Väisälä frequency, increasing GW forcing has been detected in HadGEM3 model simulations, ERA5 reanalysis, and AIRS/*Aqua* satellite observations. We have found a shift in prevailing flow regime over the Peninsula. This shift is the result of a warming surface that weakens atmospheric stability, thus allowing a larger portion of the flow approaching the mountains to rise and pass over the obstacle exciting gravity waves. We have thus demonstrated that GW forcing responds to surface stability changes on climate time scales, which implies a dependency of such a forcing on the mean climate state.

Acknowledgments. We thank Hans Hersbach for providing detailed information and statistics on the ERA5 data assimilation system used in Fig. B1. J. K. R. was supported by the Met Office Hadley Centre Climate Programme funded by DSIT. C. W. is supported by UKRI-NERC Grants NE/V01837X/1, NE/W003201/1, and NE/Z50399X/1 and by the Royal Society University Research Fellowship URF/R/221023. N.H. is supported by UKRI-NERC Grants NE/X017842/1, NE/W003201/1, and NE/Z50399X/1. This work used Monsoon2, a collaborative high-performance computing facility funded by the Met Office and the Natural Environment Research Council. Authors declare that they have no competing interests. M. V. G. designed the study, ran HadGEM3 simulations, and processed and analyzed model, reanalysis, and station data. J. K. R. ran simulations and provided access to supercomputer facilities. N. H. processed and analyzed AIRS/*Aqua* satellite data. J. K, S. C., and É. V. provided Antarctic radiosonde data. G. G. provided ERA5 reanalysis data. R. F., A. M. T., F. K., C. W., N. H., I. P., J. K., E. V., and J. R. contributed to the scientific interpretation of the results. All authors read and revised the manuscript.

Data availability statement. HadGEM3-GC3.1-LL model data for the PI and HIST simulations used in this paper are available on the CMIP6 ESGF: https://esgf-data.dkrz.de/search/cmip6-dkrz/?mip_era=CMIP6&activity_id=CMIP&institution_id=MOHC&source_id=HadGEM3-GC31-LL. Model outputs from the HadGEM3 sensitivity experiments can be accessed here: https://doi.org/10.5281/zenodo.15043790. ERA5 reanalyses are freely accessible through the Climate Data Store: Data on pressure levels are available here: https://cds.climate.copernicus.eu/datasets/reanalysis-era5-pressure-levels-monthly-means?tab=download#variable, and data on single levels are available here: https://cds.climate.copernicus.eu/datasets/reanalysis-era5-single-levels-monthly-means?tab=download. Upper-air coarse-resolution Antarctic station data can be found here: https://www.bas.ac.uk/project/reader/#data. High-resolution radiosonde data are either freely distributed by or should be requested to national

meteorological services; see Vignon et al. (2019) for details. The Unified Model is available for use through a licensing agreement; see https://www.metoffice.gov.uk/research/modelling-systems/unified-model. JULES is available under license free of charge; see https://jules.jchmr.org/. The NEMO model is available from https://www.nemo-ocean.eu. The model code for CICE can be downloaded from https://code.metoffice.gov.uk/trac/cice/browser.

APPENDIX A

Mountain Waves in Spectral Space

Var(ω) computations were carried out on selected pressure levels (500, 300, 200, 100, 50, 10, 1 hPa) and for a narrow region surrounding the Peninsula ([60°, 75°S], [70°, 35°W]) shown in Fig. A1. The input ω field (6-hourly data) was first deplaned by subtracting a least squares best-fit plane and then filtered in Fourier space to isolate mountain waves and remove wavenumbers outside of the expected range. The cutoff wavenumber k_{cf} for mountain waves was identified by inspection of 2D power spectra for typical mountain wave cases (see, as an example, Fig. A1b). All wavenumbers smaller than k_{cf} were removed from the spectrum, and the resulting filtered ω field was obtained by the inverse Fourier Transform (Fig. A1c). The filtered ω was then used to compute the variance (ω^2). The obtained Var(ω) at 6-hourly frequency was averaged spatially and finally used to compute monthly means at all the selected levels (see Fig. S15 for levels in the troposphere). Note that this approach is suitable for characterizing gravity waves from the Antarctic Peninsula in the troposphere because, at high latitudes, atmospheric convection is minimal, and the horizontal scales of mountain waves are known. Mountain waves were found to be resolved in ERA5 on horizontal scales ranging from ≈10 to 27 grid points. This is in agreement with previous studies showing that, because of hyperdiffusion, a minimum of 10 grid points are needed in ERA5 for resolving gravity waves (Preusse et al. 2014; Skamarock et al. 2014).

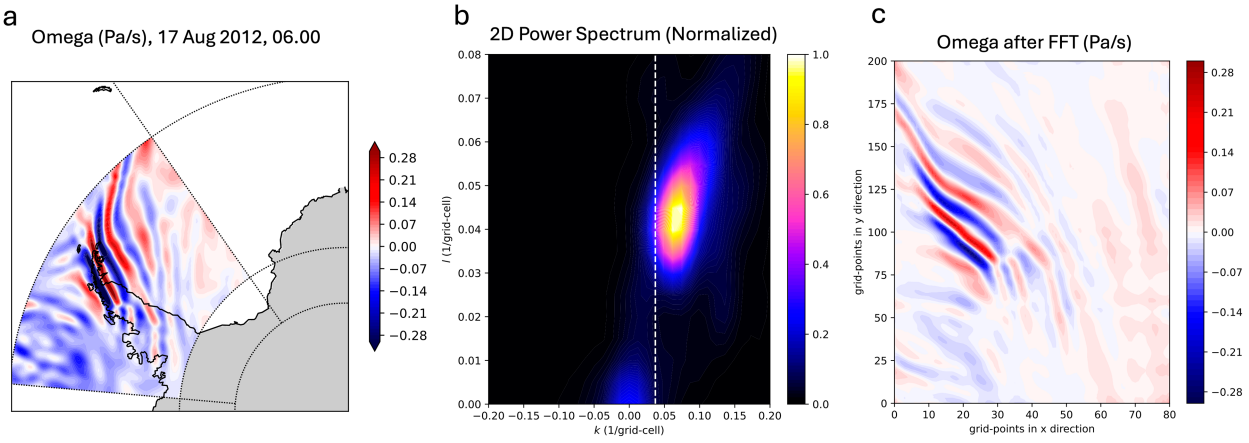

FIG. A1. (a) Vertical velocity ω from ERA5 at 100 hPa over the Antarctic Peninsula at 0600 UTC 17 Aug 2012; (b) its normalized 2D power spectrum with cutoff wavenumber (k_{cf}) for mountain waves (dashed white line); (c) the inverse Fourier transform of ω after filtering in Fourier space.

APPENDIX B

On the Reliability of Brunt–Väisälä Frequency Trends in ERA5

The first conventional observations from the Antarctic Peninsula assimilated in ERA5 date back to ≈1940. In Fig. B1, we show all conventional observations (no satellite observations) assimilated by the ERA5 4D-Var data assimilation system below 60°S since 1940. We only show locations and reference month, without specifying how many observations were there in a month or the type of records. Conventional observations include measurements made near the surface at land stations and over the ocean by ships and buoys, upper-air soundings (radiosondes and dropsondes), balloon observations, and aircraft-based atmospheric measurements. A full list can be found here: https://codes.ecmwf.int/odb/conventionalkind; for a detailed description, see Hersbach et al. (2020).

West Antarctica and the Peninsula, in particular, are the Antarctic regions where ERA5 has been constrained toward observations for the longest period and where our confidence in ERA5-derived trends is thus the highest.

A recent study by Bromwich et al. (2024) found that ERA5 surface air temperature (SAT) warming trends in Antarctica might be overall too large everywhere (Peninsula included); while this will have implications for the computation of N, the Peninsula was also found to have the most reliable long-term trends. Bromwich et al. (2024) show that ERA5 spurious warm biases in East Antarctica are likely due to the jump in temperature across the start of the modern satellite era, when data assimilation started; this is seemingly the reason why N time series for East Antarctica show a sharp decline across 1979 in Fig. S16b. Unlike the Antarctic Peninsula, observations for the Antarctic continent were sparse until the 1990s, when data assimilation over the continent interior became

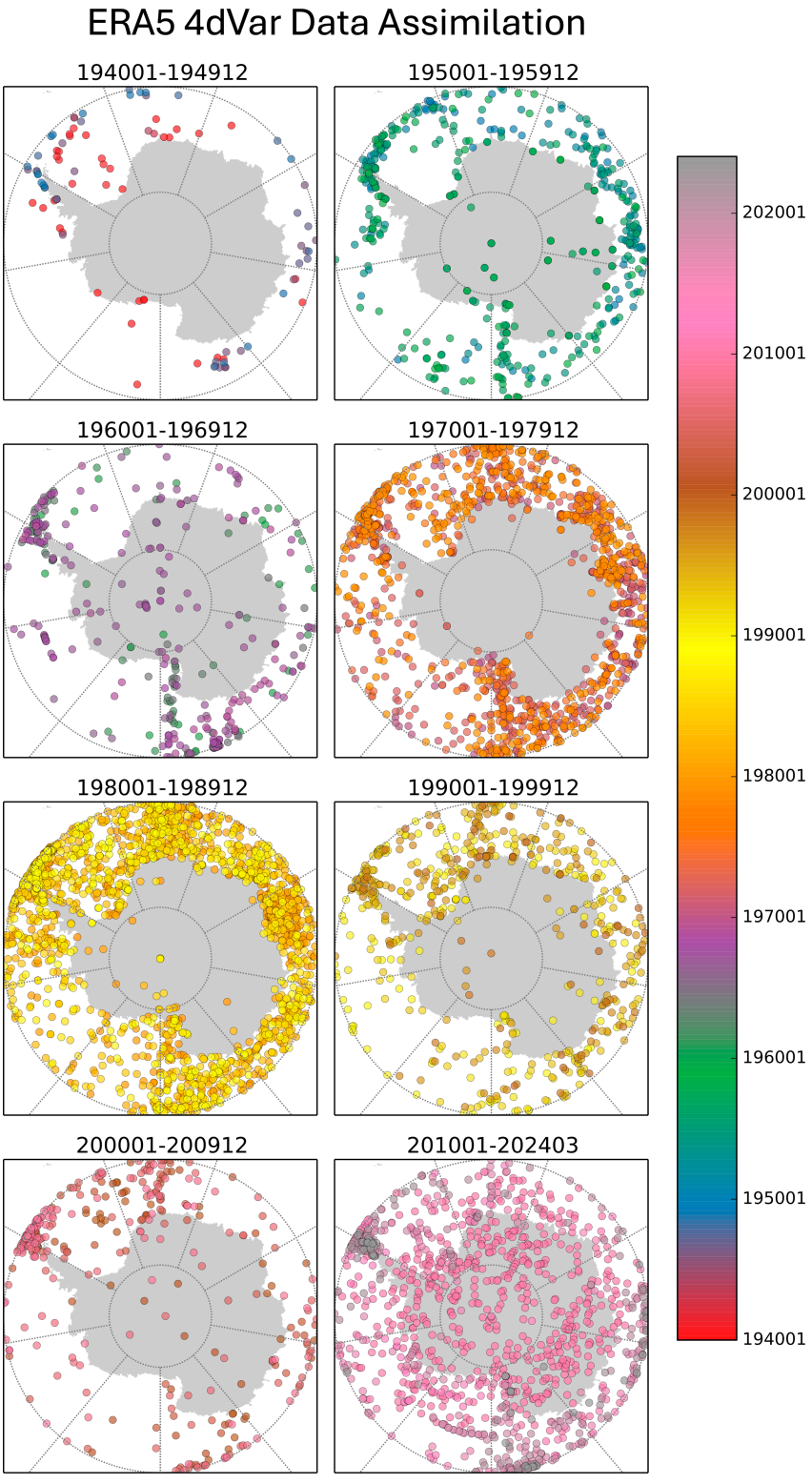

FIG. B1. Location of conventional observations assimilated by the ERA5 4D-Var data assimilation system below 60°S since 1940. Each panel contains 10 years of data with monthly frequency, and the color bar represents time.

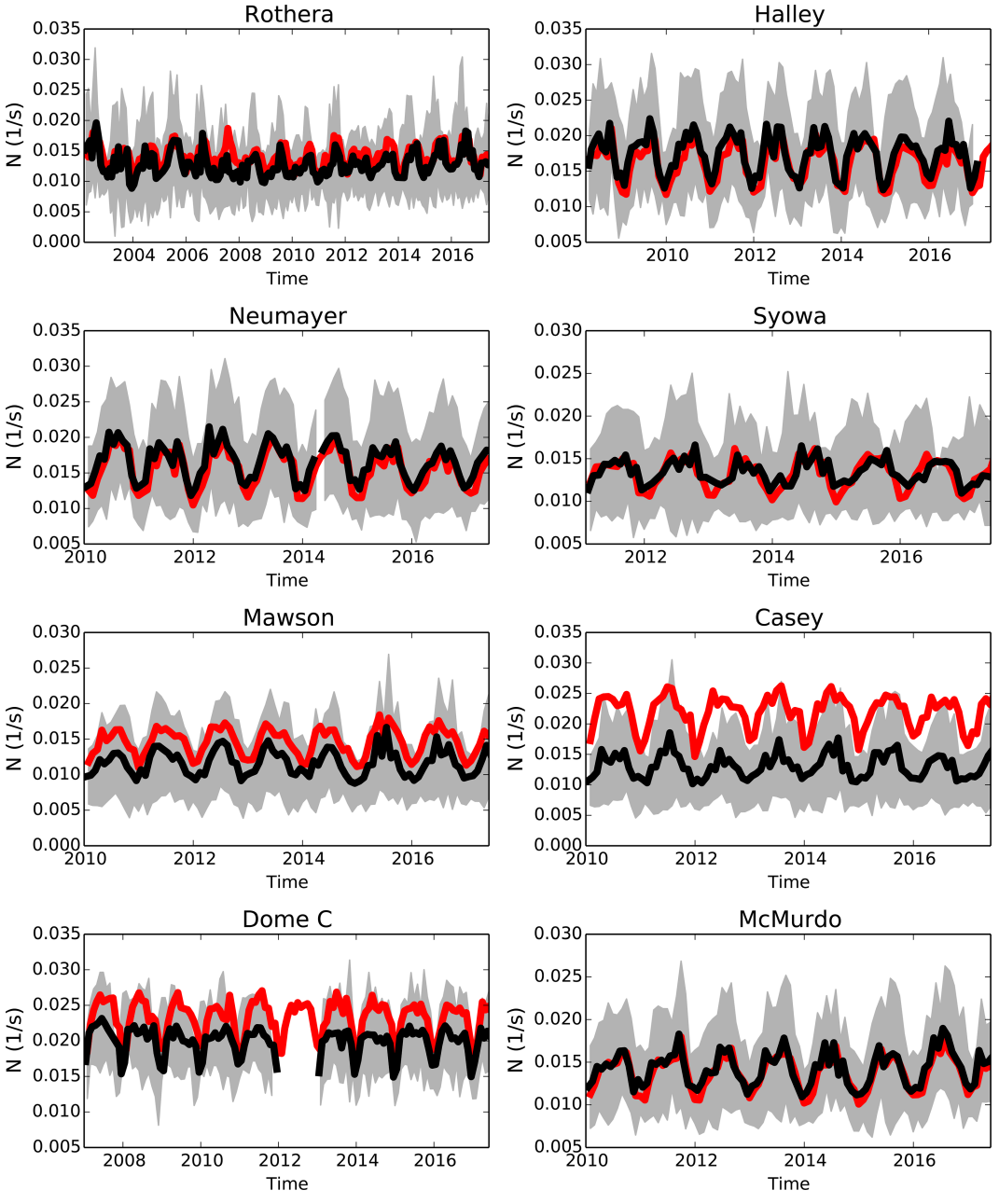

FIG. B2. Monthly mean time series of the lowest 1-km Brunt–Väisälä frequency as recorded by eight Antarctic research stations between ≈2000 and 2018 (black line) and the ERA5 simulated N at the same locations (red line). Shaded areas represent 2 times the standard deviation from the observational mean.

more consistent (Fig. B1). For this reason, we have low confidence in ERA5-derived trends for East Antarctica, which we have not discussed in this study.

A similar behavior is not observed for West Antarctica N time series (Fig. S16a) and for the Peninsula (Fig. 1). In fact, for these regions, ERA5 SAT trends were found to be in line with observations even prior to the satellite era (Bromwich et al. 2024). Further support in favor of the reliability of trends for West Antarctica comes from HadGEM3: while the model simulates a decreasing N for West Antarctica, no trends are found in the model for East Antarctica (not shown). This is due to the smaller magnitude of surface warming that the model simulates for the Antarctic continent (Fig. S7).

To assess how well ERA5 is able to reproduce the observed atmospheric stability, we used two types of observational data: high-vertical-resolution (1500 height levels) radiosonde data, only available from ≈2000s, and coarse-vertical-resolution

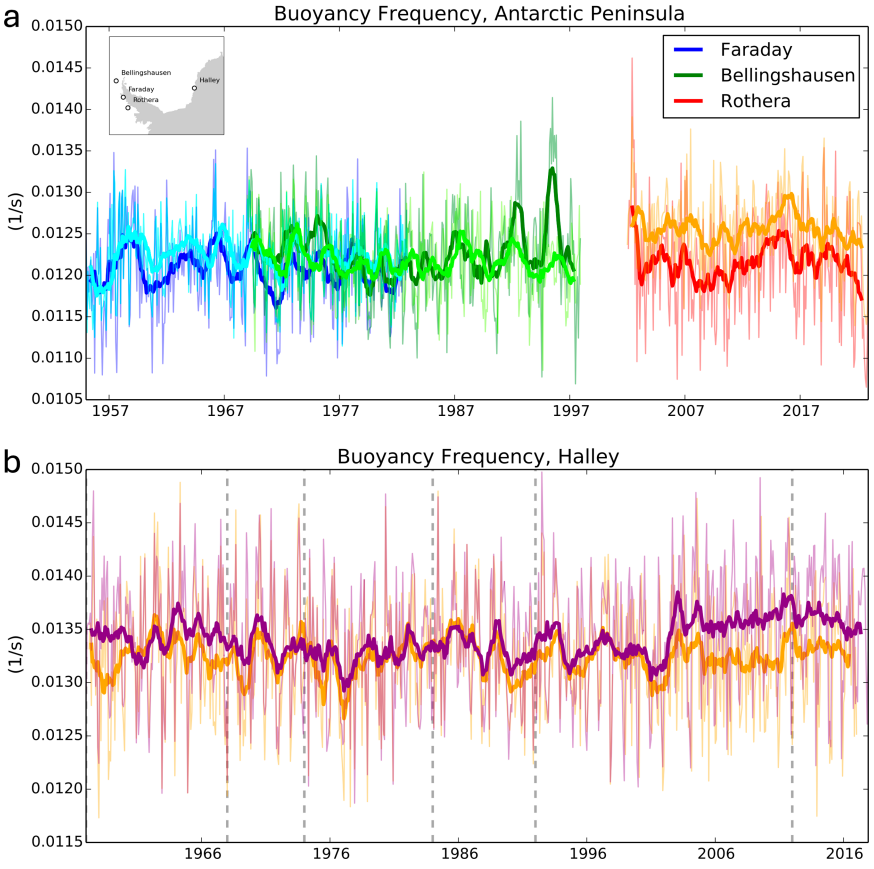

FIG. B3. (a) Observed Brunt–Väisälä frequency at 700 hPa (≈2.5 km above the surface) from radiosondes at Faraday (blue), Bellingshausen (green), and Rothera (red) research stations. ERA5 data at the same locations are shown in light green, light blue, and orange, respectively. (b) As in (a), but for Halley research station. ERA5 data are now shown in purple. Vertical dashed lines signify years in which Halley station was moved. For all panels, thin lines are monthly means, and thick lines are 12-month running means.

(nine pressure levels) radiosonde data whose recordings started in the 1950s.

High-resolution radiosonde data come from a variety of Antarctic research stations located in West and East Antarctica, as shown in Fig. S17. These data, with equally spaced vertical levels (dz = 10 m) from the surface to 15 000 m, are available only from more recent measurements (Vignon et al. 2019), and the longest record among these is from Rothera, which extends back to 2002. To reconstruct a longer record of radiosonde measurements for the Peninsula, we used coarse-resolution data (nine pressure levels from 850 to 30 hPa) from three research stations located in the northern part of Peninsula; these are Faraday (from 1955 to 1982), Bellingshausen (from 1969 to 1998), and Rothera (from 2002 to the present). We also used coarse-resolution radiosonde data from Halley (coastal East Antarctica), where measurements started in 1957 and continued to present. Measurements were collected by national Antarctic operators and are part of the Reference Antarctic Data for Environmental Research (READER) project (Turner et al. 2004).

For all research stations, we used temperature and pressure readings to compute N using (1). For high-resolution data, we excluded data points below 100 m above the surface because, within the first 100 m of the atmosphere, the balloon may have not yet reached the flow velocity (Vignon et al. 2019). The N was computed using central finite differences in the lowest 1 km of the atmosphere and then averaged vertically. If layers with superadiabatic lapse rate (i.e., negative N^2) were found, data points were masked. For coarse-resolution data, we used data at 850, 700, and 500 hPa. We computed N at ≈2.5 km (or 700 hPa) using central finite differences.

ERA5 performs remarkably well in simulating the lowest 1 km N at all considered research stations in East and West Antarctica (Fig. B2). We found that ERA5 tends to overestimate the surface N at the two research stations that are further away from the coast (Dome C and Casey), while all other stations are extremely well represented.

We also find that ERA5 is able to simulate well the atmospheric stability variability since ≈1950 (Fig. B3). At Faraday, Bellingshausen, Rothera, and Halley stations,

ERA5 reproduces closely the observed N at 700 hPa. From the 1990s onward at Bellingshausen, and from 2002 onward at Rothera, ERA5 tends to overestimate somewhat the Brunt–Väisälä frequency, while its variability continues to be well represented. However, when high-resolution data are used to compute the lowest 1 km N at Rothera for the same period of time (i.e., from 2002 onward), ERA5 performs well (Fig. B2). This is likely because, from coarse-resolution data, we can only compute N at one single level, while high-resolution data contain multiple levels and more granular information on the finer vertical structure of the Antarctic atmosphere. The coarse vertical resolution is likely also the reason why N derived from the three research stations located in the Peninsula does not show a negative trend as observed in ERA5 and HadGEM3. The N trends are large within the lowest 1 km of the atmosphere (see Fig. 2c), while N computed from station data is at 700 hPa $\approx$ 2.5 km, where static stability trends are already much weaker.

In summary, we have assessed the ability of ERA5 to reproduce the observed Brunt–Väisälä frequency and found that the reanalysis performs favorably in simulating the lowest 1 km N at all considered research stations (Fig. B2). We also found that ERA5 simulates well the variability of the atmospheric stability since $\approx$1950 (Fig. B3), as recorded by three research stations located in the northern part of the Peninsula (Faraday, Bellingshausen, and Rothera) and one in coastal East Antarctica (Halley).

REFERENCES

Alexander, S. P., A. R. Klekociuk, and T. Tsuda, 2009: Gravity wave and orographic wave activity observed around the Antarctic and Arctic stratospheric vortices by the COSMIC GPS-RO satellite constellation. *J. Geophys. Res. Atmos.*, **114**, D17103, https://doi.org/10.1029/2009JD011851.

Andrews, M. B., and Coauthors, 2020: Historical simulations with HadGEM3-GC3.1 for CMIP6. *J. Adv. Model. Earth Syst.*, **12**, e2019MS001995, https://doi.org/10.1029/2019MS001995.

Arblaster, J. M., and G. A. Meehl, 2006: Contributions of external forcings to Southern annular mode trends. *J. Climate*, **19**, 2896–2905, https://doi.org/10.1175/JCLI3774.1.

Aumann, H. H., and Coauthors, 2003: AIRS/AMSU/HSB on the aqua mission: Design, science objectives, data products, and processing systems. *IEEE Trans. Geosci. Remote Sens.*, **41**, 253–264, https://doi.org/10.1109/TGRS.2002.808356.

Bromwich, D. H., A. Ensign, S.-H. Wang, and X. Zou, 2024: Major artifacts in ERA5 2-m air temperature trends over Antarctica prior to and during the modern satellite era. *Geophys. Res. Lett.*, **51**, e2024GL111907, https://doi.org/10.1029/2024GL111907.

Carrasco, J. F., D. Bozkurt, and R. R. Cordero, 2021: A review of the observed air temperature in the Antarctic Peninsula. Did the warming trend come back after the early 21st hiatus? *Polar Sci.*, **28**, 100653, https://doi.org/10.1016/j.polar.2021.100653.

Deng, K., C. Azorin-Molina, S. Yang, C. Hu, G. Zhang, L. Minola, and D. Chen, 2022: Changes of Southern Hemisphere westerlies in the future warming climate. *Atmos. Res.*, **270**, 106040, https://doi.org/10.1016/j.atmosres.2022.106040.

Dörnbrack, A., M. Leutbecher, J. Reichardt, A. Behrendt, K.-P. Müller, and G. Baumgarten, 2001: Relevance of mountain wave cooling for the formation of polar stratospheric clouds over Scandinavia: Mesoscale dynamics and observations for January 1997. *J. Geophys. Res.*, **106**, 1569–1581, https://doi.org/10.1029/2000JD900194.

Eckermann, S. D., and Coauthors, 2016: Dynamics of orographic gravity waves observed in the mesosphere over the Auckland Islands during the Deep Propagating Gravity Wave Experiment (DEEPWAVE). *J. Atmos. Sci.*, **73**, 3855–3876, https://doi.org/10.1175/JAS-D-16-0059.1.

Elvidge, A. D., I. A. Renfrew, J. C. King, A. Orr, and T. A. Lachlan-Cope, 2016: Foehn warming distributions in nonlinear and linear flow regimes: A focus on the Antarctic Peninsula. *Quart. J. Roy. Meteor. Soc.*, **142**, 618–631, https://doi.org/10.1002/qj.2489.

Eyring, V., S. Bony, G. A. Meehl, C. A. Senior, B. Stevens, R. J. Stouffer, and K. E. Taylor, 2016: Overview of the Coupled Model Intercomparison Project Phase 6 (CMIP6) experimental design and organization. *Geosci. Model Dev.*, **9**, 1937–1958, https://doi.org/10.5194/gmd-9-1937-2016.

Garcia, R. R., A. K. Smith, D. E. Kinnison, Á. de la Cámara, and D. J. Murphy, 2017: Modification of the gravity wave parameterization in the whole atmosphere community climate model: Motivation and results. *J. Atmos. Sci.*, **74**, 275–291, https://doi.org/10.1175/JAS-D-16-0104.1.

Gonzalez, S., and D. Fortuny, 2018: How robust are the temperature trends on the Antarctic Peninsula? *Antarct. Sci.*, **30**, 322–328, https://doi.org/10.1017/S0954102018000251.

Gorodetskaya, I. V., and Coauthors, 2023: Record-high Antarctic Peninsula temperatures and surface melt in February 2022: A compound event with an intense atmospheric river. *npj Climate Atmos. Sci.*, **6**, 202, https://doi.org/10.1038/s41612-023-00529-6.

Guarino, M.-V., M. A. C. Teixeira, and M. H. P. Ambaum, 2016: Turbulence generation by mountain wave breaking in flows with directional wind shear. *Quart. J. Roy. Meteor. Soc.*, **142**, 2715–2726, https://doi.org/10.1002/qj.2862.

——, and Coauthors, 2024: A novel gravity wave transport parametrization for global chemistry climate models: Description and validation. *J. Adv. Model. Earth Syst.*, **16**, e2023MS003938, https://doi.org/10.1029/2023MS003938.

Gulev, S. K., and Coauthors, 2021: Changing state of the climate system. *Climate Change 2021: The Physical Science Basis*, V. Masson-Delmotte et al., Eds., Cambridge University Press, 287–422.

Gupta, A., T. Birner, A. Dörnbrack, and I. Polichtchouk, 2021: Importance of gravity wave forcing for springtime southern polar vortex breakdown as revealed by ERA5. *Geophys. Res. Lett.*, **48**, e2021GL092762, https://doi.org/10.1029/2021GL092762.

Hamed, K. H., and A. R. Rao, 1998: A modified Mann-Kendall trend test for autocorrelated data. *J. Hydrol.*, **204**, 182–196, https://doi.org/10.1016/S0022-1694(97)00125-X.

Hersbach, H., and Coauthors, 2020: The ERA5 global reanalysis. *Quart. J. Roy. Meteor. Soc.*, **146**, 1999–2049, https://doi.org/10.1002/qj.3803.

Hindley, N. P., C. J. Wright, N. D. Smith, L. Hoffmann, L. A. Holt, M. J. Alexander, T. Moffat-Griffin, and N. J. Mitchell, 2019: Gravity waves in the winter stratosphere over the Southern Ocean: High-resolution satellite observations and 3-D spectral analysis. *Atmos. Chem. Phys.*, **19**, 15 377–15 414, https://doi.org/10.5194/acp-19-15377-2019.

——, ——, L. Hoffmann, T. Moffat-Griffin, and N. J. Mitchell, 2020: An 18-year climatology of directional stratospheric gravity wave momentum flux from 3-D satellite observations.

Geophys. Res. Lett., **47**, e2020GL089557, https://doi.org/10.1029/2020GL089557.

Hoffmann, L., and M. J. Alexander, 2009: Retrieval of stratospheric temperatures from Atmospheric Infrared Sounder radiance measurements for gravity wave studies. *J. Geophys. Res. Atmos.*, **114**, D07105, https://doi.org/10.1029/2008JD011241.

——, X. Xue, and M. J. Alexander, 2013: A global view of stratospheric gravity wave hotspots located with atmospheric infrared sounder observations. *J. Geophys. Res. Atmos.*, **118**, 416–434, https://doi.org/10.1029/2012JD018658.

Höpfner, M., and Coauthors, 2006: MIPAS detects Antarctic stratospheric belt of NAT PSCs caused by mountain waves. *Atmos. Chem. Phys.*, **6**, 1221–1230, https://doi.org/10.5194/acp-6-1221-2006.

Hussain, M., and I. Mahmud, 2019: pyMannKendall: A python package for non parametric Mann Kendall family of trend tests. *J. Open Source Sofware*, **4**, 1556, https://doi.org/10.21105/joss.01556.

Jones, M. E., D. H. Bromwich, J. P. Nicolas, J. Carrasco, E. Plavcová, X. Zou, and S.-H. Wang, 2019: Sixty years of widespread warming in the southern middle and high latitudes (1957–2016). *J. Climate*, **32**, 6875–6898, https://doi.org/10.1175/JCLI-D-18-0565.1.

Kanehama, T., and Coauthors, 2022: Evaluation and optimizaton of orographic drag in the IFS. ECMWF Tech. Memo. 893, 33 pp.

King, J. C., and Coauthors, 2017: The impact of Föhn winds on surface energy balance during the 2010–2011 melt season over Larsen C Ice Shelf, Antarctica. *J. Geophys. Res. Atmos.*, **122**, 12 062–12 076, https://doi.org/10.1002/2017JD026809.

Kirchgaessner, A., J. C. King, and P. S. Anderson, 2021: The impact of Föhn conditions across the Antarctic Peninsula on local meteorology based on AWS measurements. *J. Geophys. Res. Atmos.*, **126**, e2020JD033748, https://doi.org/10.1029/2020JD033748.

Kuhlbrodt, T., and Coauthors, 2018: The low-resolution version of HadGEM3 GC3.1: Development and evaluation for global climate. *J. Adv. Model. Earth Syst.*, **10**, 2865–2888, https://doi.org/10.1029/2018MS001370.

Lim, E.-P., H. H. Hendon, G. Boschat, D. Hudson, D. W. Thompson, A. J. Dowdy, and J. M. Arblaster, 2019: Australian hot and dry extremes induced by weakenings of the stratospheric polar vortex. *Nat. Geosci.*, **12**, 896–901, https://doi.org/10.1038/s41561-019-0456-x.

Lott, F., and M. J. Miller, 1997: A new subgrid-scale orographic drag parametrization: Its formulation and testing. *Quart. J. Roy. Meteor. Soc.*, **123**, 101–127, https://doi.org/10.1256/smsqj.53703.

Madec, G., 2015: *NEMO Ocean Engine.* Institut Pierre-Simon Laplace, 391 pp.

Marshall, G. J., A. Orr, N. P. van Lipzig, and J. C. King, 2006: The impact of a changing Southern Hemisphere Annular Mode on Antarctic Peninsula summer temperatures. *J. Climate*, **19**, 5388–5404, https://doi.org/10.1175/JCLI3844.1.

McLandress, C., T. G. Shepherd, S. Polavarapu, and S. R. Beagley, 2012: Is missing orographic gravity wave drag near 60°S the cause of the stratospheric zonal wind biases in chemistry–climate models? *J. Atmos. Sci.*, **69**, 802–818, https://doi.org/10.1175/JAS-D-11-0159.1.

Menary, M. B., and Coauthors, 2018: Preindustrial control simulations with HadGEM3-GC3.1 for CMIP6. *J. Adv. Model. Earth Syst.*, **10**, 3049–3075, https://doi.org/10.1029/2018MS001495.

Miranda, P. M. A., and I. N. James, 1992: Non-linear three-dimensional effects on gravity-wave drag: Splitting flow and breaking waves. *Quart. J. Roy. Meteor. Soc.*, **118**, 1057–1081, https://doi.org/10.1256/smsqj.50802.

Nappo, C. J., 2013: *An Introduction to Atmospheric Gravity Waves.* Vol. 102. Academic Press, 359 pp.

Orr, A., G. J. Marshall, J. C. R. Hunt, J. Sommeria, C.-G. Wang, N. P. M. van Lipzig, D. Cresswell, and J. C. King, 2008: Characteristics of summer airflow over the Antarctic Peninsula in response to recent strengthening of westerly circumpolar winds. *J. Atmos. Sci.*, **65**, 1396–1413, https://doi.org/10.1175/2007JAS2498.1.

——, and Coauthors, 2015: Inclusion of mountain-wave-induced cooling for the formation of PSCs over the Antarctic Peninsula in a chemistry–climate model. *Atmos. Chem. Phys.*, **15**, 1071–1086, https://doi.org/10.5194/acp-15-1071-2015.

Preusse, P., M. Ern, P. Bechtold, S. D. Eckermann, S. Kalisch, Q. T. Trinh, and M. Riese, 2014: Characteristics of gravity waves resolved by ECMWF. *Atmos. Chem. Phys.*, **14**, 10 483–10 508, https://doi.org/10.5194/acp-14-10483-2014.

Reinecke, P. A., and D. R. Durran, 2008: Estimating topographic blocking using a Froude number when the static stability is nonuniform. *J. Atmos. Sci.*, **65**, 1035–1048, https://doi.org/10.1175/2007JAS2100.1.

Ridley, J. K., E. W. Blockley, A. B. Keen, J. G. L. Rae, A. E. West, and D. Schroeder, 2018: The sea ice model component of HadGEM3-GC3.1. *Geosci. Model Dev.*, **11**, 713–723, https://doi.org/10.5194/gmd-11-713-2018.

Sandu, I., P. Bechtold, A. Beljaars, A. Bozzo, F. Pithan, T. G. Shepherd, and A. Zadra, 2016: Impacts of parameterized orographic drag on the Northern Hemisphere winter circulation. *J. Adv. Model. Earth Syst.*, **8**, 196–211, https://doi.org/10.1002/2015MS000564.

Sen, P. K., 1968: Estimates of the regression coefficient based on Kendall's tau. *J. Amer. Stat. Assoc.*, **63**, 1379–1389, https://doi.org/10.2307/2285891.

Simmonds, I., 2015: Comparing and contrasting the behaviour of Arctic and Antarctic Sea ice over the 35 year period 1979–2013. *Ann. Glaciol.*, **56**, 18–28, https://doi.org/10.3189/2015AoG69A909.

——, and E.-P. Lim, 2009: Biases in the calculation of Southern Hemisphere mean baroclinic eddy growth rate. *Geophys. Res. Lett.*, **36**, L01707, https://doi.org/10.1029/2008GL036320.

——, and M. Li, 2021: Trends and variability in polar sea ice, global atmospheric circulations, and baroclinicity. *Ann. N. Y. Acad. Sci.*, **1504**, 167–186, https://doi.org/10.1111/nyas.14673.

Skamarock, W. C., S.-H. Park, J. B. Klemp, and C. Snyder, 2014: Atmospheric kinetic energy spectra from global high-resolution nonhydrostatic simulations. *J. Atmos. Sci.*, **71**, 4369–4381, https://doi.org/10.1175/JAS-D-14-0114.1.

Smith, R. B., 1977: The steepening of hydrostatic mountain waves. *J. Atmos. Sci.*, **34**, 1634–1654, https://doi.org/10.1175/1520-0469(1977)034<1634:TSOHMW>2.0.CO;2.

——, 1980: Linear theory of stratified hydrostatic flow past an isolated mountain. *Tellus*, **32** (4), 348–364, https://doi.org/10.3402/tellusa.v32i4.10590.

——, 1989: Mountain-induced stagnation points in hydrostatic flow. *Tellus*, **41A**, 270–274, https://doi.org/10.3402/tellusa.v41i3.11839.

Soci, C., and Coauthors, 2024: The ERA5 global reanalysis from 1940 to 2022. *Quart. J. Roy. Meteor. Soc.*, **150**, 4014–4048, https://doi.org/10.1002/qj.4803.

Teixeira, M. A. C., 2014: The physics of orographic gravity wave drag. *Front. Phys.*, **2**, 43, https://doi.org/10.3389/fphy.2014.00043.

Theil, H., 1950: A rank-invariant method of linear and polynomial regression analysis. *Indagationes Math.*, **12**, 173.

Thompson, D. W. J., and S. Solomon, 2002: Interpretation of recent Southern Hemisphere climate change. *Science*, **296**, 895–899, https://doi.org/10.1126/science.1069270.

Turner, J., and Coauthors, 2004: The SCAR READER project: Toward a high-quality database of mean Antarctic meteorological observations. *J. Climate*, **17**, 2890–2898, https://doi.org/10.1175/1520-0442(2004)017<2890:TSRPTA>2.0.CO;2.

——, G. J. Marshall, K. Clem, S. Colwell, T. Phillips, and H. Lu, 2020: Antarctic temperature variability and change from station data. *Int. J. Climatol.*, **40**, 2986–3007, https://doi.org/10.1002/joc.6378.

VanZandt, T. E., and D. C. Fritts, 1989: A theory of enhanced saturation of the gravity wave spectrum due to increases in atmospheric stability. *Pure Appl. Geophys.*, **130**, 399–420, https://doi.org/10.1007/BF00874466.

Vignon, É., O. Traullé, and A. Berne, 2019: On the fine vertical structure of the low troposphere over the coastal margins of east Antarctica. *Atmos. Chem. Phys.*, **19**, 4659–4683, https://doi.org/10.5194/acp-19-4659-2019.

——, G. Picard, C. Durán-Alarcón, S. P. Alexander, H. Gallée, and A. Berne, 2020: Gravity wave excitation during the coastal transition of an extreme katabatic flow in Antarctica. *J. Atmos. Sci.*, **77**, 1295–1312, https://doi.org/10.1175/JAS-D-19-0264.1.

Virtanen, P., and Coauthors, 2020: SciPy 1.0: Fundamental algorithms for scientific computing in Python. *Nat. Methods*, **17**, 261–272, https://doi.org/10.1038/s41592-019-0686-2.

Walters, D., and Coauthors, 2017: The Met Office Unified Model global atmosphere 6.0/6.1 and JULES global land 6.0/6.1 configurations. *Geosci. Model Dev.*, **10**, 1487–1520, https://doi.org/10.5194/gmd-10-1487-2017.

Williams, K. D., and Coauthors, 2018: The Met Office Global Coupled Model 3.0 and 3.1 (GC3.0 and GC3.1) configurations. *J. Adv. Model. Earth Syst.*, **10**, 357–380, https://doi.org/10.1002/2017MS001115.